Oblique Wave Effects on the Hydrodynamic Responses of Side-by-Side Moored FLNG and LNGC

Ke Zhou[1]; Zhiqiang Hu[2]; Dongya Zhao[3]; Decheng Wan[4]; and Xiangyin Meng[5]

Abstract: The motion response predictions of side-by-side moored floating liquefied natural gas (FLNG) and liquefied natural gas carrier (LNGC) under oblique waves is critically important to validate operational security. This article studies the hydrodynamic interactions of side-by-side moored FLNG + LNGC under oblique waves by both numerical simulation and model testing. The artificial damping method, calibrated through gap wave elevations measured in model tests, is adopted to simulate the viscous effect in the gap region using the state-of-the-art software HydroStar. The hydrodynamic performances of the side-by-side system under oblique waves are investigated. Relative motions under different wave directions are also investigated, and the resonant phenomena are analyzed through phase shift. The investigations indicate that motion responses of FLNG are less affected by wave directions, whereas the motions of LNGC at the lee side are suppressed due to the shielding effect of FLNG. Relative motions between FLNG and LNGC tend to be amplified with the out-of-phase mode when two vessels oscillate in the opposed directions, induced by gap water resonances at high frequencies, whereas the mode of relative motions induced by roll resonance depends on wave directions and resonance frequencies. **DOI: 10.1061/(ASCE)WW.1943-5460.0000457.**

Author keywords: Floating liquefied natural gas (FLNG); Hydrodynamic interactions; Oblique wave; Shielding effect; Gap water resonance.

Introduction

With the development of natural gas exploitation from offshore stranded gas reserves, floating liquefied natural gas (FLNG) has attracted considerable attention as an effective platform for exploitation, processing, and storage of natural gas in remote offshore areas. Instead of a conventional method of gas transportation through long pipelines, the cryogenic nature of liquefied natural gas (LNG) determines a small distance between FLNG and liquefied natural gas carrier (LNGC) with a side-by-side configuration in offloading operation. Nevertheless, the side-by-side offloading under unexpected weather conditions, in particular occasional oblique waves, might induce high risks of collision and large motions of vessels. Thus, it is necessary to implement an accurate prediction of side-by-side vessel motions to ensure safe operability. The objective of the present research is to experimentally and numerically analyze the hydrodynamic performances of side-by-side FLNG and LNGC under various oblique wave sea states.

There are two problems when predicting the motion of parallel arranged vessels in close proximity: hydrodynamic interactions between floating bodies and the viscous effect of gap water in between. Both problems have been studied by many researchers.

For frequency-domain analysis of multibody hydrodynamic interactions, Ohkusu (1969) first applied the two-dimensional (2D) strip theory to the calculation of hydrodynamic parameters of two circular cylinders and Kodan (1984) subsequently measured the motions of a parallel barge and ship in waves and compared the 2D results with test results. As computational ability improved, a three-dimensional (3D) method based on Green's function was introduced for multibody calculation. Van Oortmerssen (1979) performed numerical studies for floating vertical cylinders and barges in heading wave conditions and compared the numerical results with the experimental results. Fang and Chen (2001) investigated the relative motions and wave elevations between two bodies and obtained satisfactory agreement between numerical and experiment results. Lewandowski (2008) compared the 3D boundary element method with the 2D method in the calculation of hydrodynamic parameters of twin barges in close proximity and confirmed the profound influence on the hydrodynamic forces and responses of the bodies near the critical frequencies due to resonant behavior of the water in the gap. The higher order boundary element method (HOBEM) has been used by Choi and Hong (2002) to investigate the hydrodynamic interactions of a floating multibody system, including motion responses and wave drift forces, for the sake of computational efficiency and convergence. Sun et al. (2015) used first- and second-order diffraction analyses to study hydrodynamic interactions and captured the intense fluid motions within the gap between the two vessels, which are all fixed or free-floating. Xu et al. (2016) investigated

[1]Postgraduate Student, State Key Laboratory of Ocean Engineering, Shanghai Jiao Tong Univ., 800 Dongchuan Rd., Shanghai 200240, China. Email: 115010910136@sjtu.edu.cn

[2]Senior Lecturer, School of Engineering, Newcastle Univ., Newcastle upon Tyne, NE1 7RU, UK (corresponding author). Email: zhiqiang.hu@ncl.ac.uk

[3]Ph.D. Student, State Key Laboratory of Ocean Engineering, Shanghai Jiao Tong Univ., 800 Dongchuan Rd., Shanghai 200240, China. Email: zhaoraul@sjtu.edu.cn

[4]Professor, School of Naval Architecture Ocean & Civil Engineering, Shanghai Jiao Tong Univ., 800 Dongchuan Rd., Shanghai 200240, China. Email: dcwan@sjtu.edu.cn

[5]Teaching Fellow, School of Engineering, Newcastle Univ., Newcastle upon Tyne, NE1 7RU, UK. Email: xiangyin.meng@ncl.ac.uk

Note. This manuscript was submitted on August 21, 2017; approved on February 1, 2018; published online on April 26, 2018. Discussion period open until September 26, 2018; separate discussions must be submitted for individual papers. This paper is part of the ***Journal of Waterway, Port, Coastal, and Ocean Engineering***, © ASCE, ISSN 0733-950X.

the hydrodynamic interactions among three side-by-side barges with both low-order and high-order boundary element methods. The mean drift force of each barge in a head sea was evaluated with near-field and middle-field methods to draw a comparison with the experimental results.

For time-domain analysis, extensive study has been done based on the impulse response function following the original formulation of Cummins (1962). Buchner et al. (2001) developed the numerical time-domain simulation model to predict the motion response of FPSO LNG with an alongside moored LNG carrier, which was validated by basin model tests. Kim et al. (2008) adopted the 3D Rankine panel method to study the motion responses of multiple adjacent floating bodies in the time domain. Configurations of two adjacent Series 60 hulls and a ship–barge model in oblique waves were investigated, and numerical simulation was consolidated with experimental results. Zhao et al. (2014) investigated the hydrodynamic characteristics of the side-by-side moored FLNG and LNGC connected by hawsers and fenders using a time-domain simulation code SIMO and validated the ship motions and loads on hawsers and fenders with test results. Watai et al. (2015) studied the seakeeping problem of two ships in side-by-side configuration and improved the convergence of the time-domain Rankine panel method by incorporating the artificial damping method.

As studied by previous research, classical potential theory always overestimates the fluid motion at certain spaced frequencies corresponding to the wave resonance in the gap. Molin (2001) did the pioneering research on the wave propagation in a channel as a simplified model of the gap wave resonance problem. The resonance frequencies and free-surface modal shapes between twin floaters were further studied by Yeung and Seah (2007). Recent research (Pessoa et al. 2015; Shivaji and Sen 2016) indicated that the gap can be treated as a longitudinally unbounded moonpool sharing similar resonant modes, although not identical, with the canonical ones for moonpools including the pumping mode and sloshing modes (Molin 2001). The viscous effect of wave resonance in the gap should not be ignored due to the viscous dissipative effect that actually takes place near the bilge keels via flow separation and on the vessel walls due to friction. Many scholars have adapted the inviscid potential theory by introducing certain damping mechanisms to control the unrealistic wave elevations and fluid motions. A "rigid lid method" was first proposed by Huijsmans et al. (2001) to fully stifle the wave elevations in the gap and applied by Buchner et al. (2001) in his study of a side-by-side offloading system to press down drastic wave resonance. To allow a wavy motion of the lid, Newman (2004) rendered the "flexible lid" whose deformation equals the free-surface elevation and is described by a set of Chebyshev polynomials as the basis functions. A damping coefficient is then introduced to reduce lid deformation. Both methods bring about the disturbance of the real flow field around hulls and only serve as a basic approximation of the viscous effect.

Unlike the methods previously mentioned, Chen (2005) applied directly a linear damping force into the original equation to emulate the nature of energy dissipation in the flow field. A modified free-surface condition is derived based on the linear damping coefficient epsilon (ε) and plays an important role in predicting the behavior of water in the confined zone. The damping coefficient could be selected through matching the computed results with testing results in terms of wave elevations or second-order quantities. Extensive study has been done to investigate the effectiveness of this artificial damping method. Fournier et al. (2006) validated the function of the artificial damping in which a single linear damping coefficient tuned by experiment shows good correspondence in terms of wave elevations, ship motion response amplitude operators (RAOs), and mean drift force transfer functions in head seas. However, Pauw et al. (2007) complemented that, for a narrow gap (less than one-tenth of vessel breadth in the literature), no single value of artificial damping could fully cover all the first-order quantities and the value should be tuned according to second-order test results, such as wave drift forces. Bunnik et al. (2009) suggested the artificial damping on the interior body surface to eliminate irregular frequencies instead of the conventional rigid lid method, which shows a strong mesh dependency.

Model tests on the hydrodynamics of the side-by-side configuration have been applied for over a decade. To validate the time-domain calculation of multibody hydrodynamic interactions, Buchner et al. (2001) performed model tests for coupled and uncoupled side-by-side vessels in close proximity. Hong et al. (2002) conducted model tests for side-by-side tankers to investigate the hydrodynamic interactions between two vessels with respect to their motion responses and drift forces in head sea and beam sea conditions. To provide insight into the relative motions and the forces in the mooring lines between two hulls, Van der Valk and Watson (2005) implemented a comprehensive set of basin model tests under multidirectional wave climates and recommended that a full dynamic positioning might be preferred over the physical mooring arrangement in severe environments. Pauw et al. (2007) performed the model test with the LNGC along the basin wall under both free and fixed modes to obtain the value of the damping parameter. Model tests of side-by-side moored FLNG and LNGC were also performed by Zhao et al. (2014) in the deepwater offshore basin at Shanghai Jiao Tong University, China, for a better understanding of the hydrodynamic characteristics. The numerical method based on the time-domain code SIMO was also validated.

In this study, hydrodynamic analysis of a side-by-side offloading system was performed under different oblique waves, using the state-of-the-art software HydroStar for frequency-domain calculation and an in-house code to implement the time-domain simulation of this multibody system. The artificial damping method (Chen 2005) was used to simulate the viscous effect between closely arranged vessels and modify the motion responses in the vicinity of gap resonance frequencies. Model tests were performed to tune the damping coefficient ε based on wave elevations within the gap. Based on the finely tuned ε, the hydrodynamic performances of the side-by-side system under oblique wave conditions were studied by comparing numerical results and test results. Subsequently, the motion responses under different wave directions were compared and analyzed to reveal the influence of wave directions. Finally, relative motions were calculated with the developed in-house code in time domain and compared with experimental results.

Mathematical Formulation

This article aims at investigating the hydrodynamic couplings between side-by-side FLNG and LNGC systems under oblique waves. Two free-floating vessels are set parallel with a gap width of 6 m. The mathematical formulation describing this problem will be deducted in this section followed by its solving method in both frequency and time domain.

Coordinate System

To describe the hydrodynamic problem, three coordinate systems are established (Fig. 1), including two reference coordinate systems

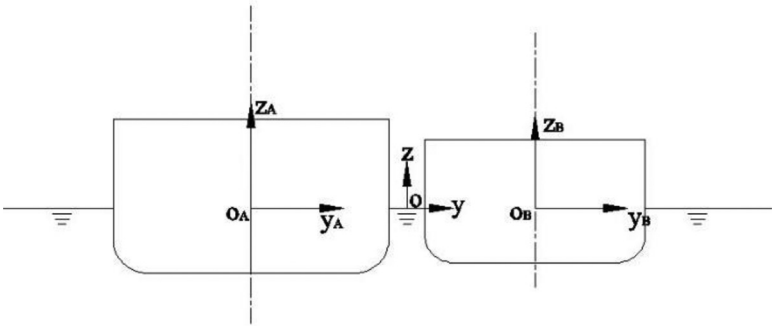

Fig. 1. Definition of coordinate systems.

with subscripts of A or B to represent FLNG and LNGC, respectively, as well as the global coordinate system.

The origin of each reference system is fixed at the center point of the water plane. The global system origin is fixed at the center point of the gap surface. The x-axis directs positively toward the ship bow, whereas the z-axis directs vertically upward. Regarding this double-body problem, 12 (2×6) degrees of freedom (DOF) termed as generalized modes need to be considered to describe the motion of two vessels in space.

Governing Equations and Boundary Conditions

Based on the incompressible and inviscid potential flow, the velocity potential satisfies the Laplace equation in fluid domain

$$\nabla^2 \Phi = 0 \tag{1}$$

Based on the small amplitude wave assumption and perturbation procedure, the linearized boundary value problem can be derived and solved. The fluid motion is assumed to be harmonic in time with the circular frequency ω. The total periodic velocity potential in the form of sinusoidal oscillation can be expressed as

$$\Phi(x,y,z,t) = \mathrm{Re}\left\{\left[\eta_w(\phi_I + \phi_D) + \sum_{j=1}^{12} \overline{\xi}_j \phi_j\right] e^{-i\omega t}\right\} \tag{2}$$

where η_w = wave amplitude; $\overline{\xi}_j$ = complex amplitude of jth mode motion; ϕ_I = incident potential; ϕ_D = diffraction potential induced by the presence of bodies in waves; and $\phi_j (j = 1, 2, ...12)$ represents the radiation potentials induced by forced motions in still water. The linear boundary conditions satisfied by velocity potentials $\phi_m (m = D \text{ or } j)$ in the frequency domain are as follows:

1. Linear free-surface condition

$$-\omega^2 \phi_m + g \frac{\partial}{\partial z} \phi_m = 0, \ z = 0 \tag{3}$$

2. Sea bed condition

$$\frac{\partial}{\partial n} \phi_m = 0, \ z = -h \tag{4}$$

3. Body-surface condition for diffraction potential

$$\frac{\partial \phi_D}{\partial n} = -\frac{\partial \phi_I}{\partial n}, \text{ on } H_1 \cup H_2 \tag{5}$$

4. Body-surface condition for radiation potential [Eqs. (6*a*)–(6*d*)]

$$\frac{\partial}{\partial n} \phi_j = n_j \ (j = 1, 2, ...6) \quad \text{on } H_1$$

$$\frac{\partial}{\partial n} \phi_j = 0 \ \ (j = 1, 2, ...6) \quad \text{on } H_2$$

$$\frac{\partial}{\partial n} \phi_j = n_j \ \ (j = 7, 8, ...12) \quad \text{on } H_2$$

$$\frac{\partial}{\partial n} \phi_j = 0 \ \ (j = 7, 8, ...12) \quad \text{on } H_1 \tag{6a–d}$$

5. Radiation condition in the far field

$$\lim_{R \to \infty} \sqrt{R}\left(\frac{\partial \phi_m}{\partial R} - ik\phi_m\right) = 0, \ R = \sqrt{x^2 + y^2} \tag{7}$$

where h = water depth; k = wave number, which satisfies the dispersion relation $\omega^2 = gk \tanh(kh)$; H_1 and H_2 represent the body boundaries of FLNG and LNGC, respectively; and $(n_1, n_2, n_3) = \overrightarrow{n}$, $(n_4, n_5, n_6) = (x_1, y_1, z_1) \times \overrightarrow{n}$, and $\overrightarrow{n}$ are the unit vector normals to the body boundary.

Artificial Damping Method

The artificial damping method (Chen 2005) derives from the modification of inviscid potential flow by introducing a fictitious force dependent on the fluid velocity in the momentum equation

$$\boldsymbol{f}_{dmp} = -\mu \boldsymbol{V} \tag{8}$$

where $\boldsymbol{V}$ = velocity of water particles; and μ is defined as a damping factor. Hence, the modified momentum equation is

$$\boldsymbol{V} \nabla \bullet \boldsymbol{V} + \frac{\partial \boldsymbol{V}}{\partial t} = -\mu \boldsymbol{V} + \boldsymbol{f} + \frac{1}{\rho} \nabla P \tag{9}$$

where $\boldsymbol{f}$ = inertia force (gravity here), whereas P = fluid pressure. Because this fictitious force does not introduce any vorticity, although incorporating the viscous effect of fluid motion, the existence of velocity potential is safeguarded. Bernoulli's equation derived from Eq. (9) can be expressed as

$$\frac{P}{\rho} + gz + \frac{\partial \Phi}{\partial t} + \frac{\nabla \Phi \bullet \nabla \Phi}{2} + \mu \Phi = 0 \tag{10}$$

where ρ = water density; and g = acceleration of gravity. Ignoring the second-order item, the wave elevation can be expressed as

$$\eta = -\frac{1}{g}\left(\frac{\partial \Phi}{\partial t} + \mu \Phi\right) \tag{11}$$

For the linear boundary value problem, the free-surface condition can be expressed as

$$g\frac{\partial \Phi}{\partial z}+\frac{\partial^2 \Phi}{\partial t^2}+\mu\Phi=0 \tag{12}$$

Hence, the conventional free-surface condition in Eq. (3) can be modified as

$$-(1+i\varepsilon)\omega^2\phi_m+g\frac{\partial}{\partial z}\phi_m=0,\ \frac{\mu}{\omega}=\varepsilon \tag{13}$$

where ε represents the artificial damping coefficient ranging from 0 to 1. When $\varepsilon=0$, this boundary condition degrades into the conventional one as seen in Eq. (3). When $\varepsilon=1$, the equivalent effect of the rigid lid is achieved to suppress any free-surface motion.

Frequency-Domain Solution

The previously mentioned first-order boundary value problem can be solved using the source distribution method. The radiation and diffraction potential can be expressed by an integral of source distribution on the boundaries consisting of all body surfaces H and free-surface F as follows:

$$\phi(P)=\iint_S dS\sigma(Q)G(P,Q), S=H\cup F \tag{14}$$

where $\sigma(Q)$ = source density of source Point Q on the boundaries; $G(P,Q)$ is the Green's function standing for the potential at field Point P induced by the source of unit density at Point Q; H is the assemble of all body surfaces ($H_1\cup H_2$); and F = entire free surface.

Considering the rectified free-surface condition in Eq. (13), the source distribution $\sigma(P)$ is determined by satisfying not only the boundary conditions on hull H, but also on the free-surface F, as follows:

$$2\pi\sigma(P)+\iint_S dS\sigma(Q)\frac{\partial}{\partial n}G(P,Q)=\nu_n, p\subset H \tag{15}$$

$$4\pi\sigma(P)+i\varepsilon k\iint_S dS\sigma(Q)G(P,Q)=0, p\subset F \tag{16}$$

Boundary conditions vary for different problems. For the diffraction potential calculation, $\nu_n=-\partial\phi_I/\partial n$, and for the radiation potential calculation, $\nu_n=n_j$. For the purpose of suppressing unrealistic wave elevations only between two bodies, it is appropriate to apply a nonzero ε onto the confined damping zone and leave $\varepsilon=0$ on the outer free surface. The size of the slender damping zone and the spatial distribution of ε value are still uncertain.

Once the integral equations are solved, wave forces applied on the vessels can be achieved through the integral of hydrodynamic pressure over the body surfaces. The linear and harmonic motions of floating bodies are evaluated by solving a coupled motion equation at the wave frequency ω

$$\left[-\omega^2(\boldsymbol{M}+\boldsymbol{a})-i\omega(\boldsymbol{b}+\boldsymbol{b}')+\boldsymbol{K}\right]\boldsymbol{\xi}=\boldsymbol{F} \tag{17}$$

where $\boldsymbol{M}$ is the generalized mass matrix; $\boldsymbol{a}$ and $\boldsymbol{b}$ are the added mass and potential damping coefficient matrix; b' is the linear viscous damping matrix, which is derived from decay tests (Zhao et al. 2013); $\boldsymbol{K}$ is the hydrostatic restoring force matrix; $\boldsymbol{\xi}$ is the motion response vector of two vessels; and $\boldsymbol{F}$ is the wave exciting force vector, which consists of the F-K force and diffraction force. Note that all the formulas presented here correspond to the theories used in the software HydroStar for frequency-domain calculation.

Time-Domain Solution

A time-domain simulation is adopted to further simulate the hydrodynamic couplings between side-by-side vessels. Based on the impulse response theory by Cummins (1962), the coupled equation in time domain can be written as

$$[\boldsymbol{M}+\boldsymbol{a}(\infty)]\{\ddot{\xi}(t)\}+\int_0^t[\boldsymbol{h}(t-\tau)]\{\dot{\xi}(t)\}d\tau+\boldsymbol{C}_{\text{vis}}\{\dot{\xi}(t)\}+\boldsymbol{K}\{\xi(t)\}=\boldsymbol{F}(t) \tag{18}$$

where $\boldsymbol{M}$ and $\boldsymbol{K}$ have been defined previously in Eq. (17); $\boldsymbol{a}(\infty)$ is the added mass matrix at infinite frequency; $\boldsymbol{C}_{\text{vis}}$ is the linear damping matrix; $\xi(t)$ indicates the displacement vector of the vessels; $\boldsymbol{F}(t)$ denotes the vector of wave force time traces converted from frequency-domain diffraction results through fast Fourier transform (FFT); and $\boldsymbol{h}(\tau)$ signifies the retardation function matrix, representing the memory effect of the free surface on the subsequent ship motions. It can be achieved from the reverse Fourier transformation of frequency-domain coefficients as follows:

$$\boldsymbol{h}(\tau)=\frac{2}{\pi}\int_0^\infty \boldsymbol{b}(\omega)\cos\omega\tau d\omega=-\frac{2}{\pi}\int_0^\infty \omega[\boldsymbol{a}(\omega)-\boldsymbol{a}(\infty)]\sin\omega\tau d\omega \tag{19}$$

where $\boldsymbol{a}$ and $\boldsymbol{b}$ are the added mass matrix and radiation damping matrix obtained from the frequency-domain calculation.

In this study, frequency-domain damping coefficients modified by the artificial damping method are used to calculate the retardation function. Because asymptotic behavior causes damping coefficients to approach zero at infinite frequencies, high-frequency truncation would yield adequately accurate retardation function.

A fully coupled model is used in this calculation considering hydrodynamic interactions; in that case the inertia term $[\boldsymbol{M}+\boldsymbol{a}(\infty)]$ can be expanded as

$$\begin{bmatrix}(\boldsymbol{M}+\boldsymbol{a}(\omega))_{ii} & \boldsymbol{a}(\omega)_{ij}\\ \boldsymbol{a}(\omega)_{ji} & (\boldsymbol{M}+\boldsymbol{a}(\omega))_{jj}\end{bmatrix}\begin{Bmatrix}\ddot{\xi}_i\\ \ddot{\xi}_j\end{Bmatrix} \tag{20}$$

where the indices i and j refer to body i and body j. The convolution term can be expanded as

$$\int_0^t\begin{bmatrix}\boldsymbol{h}(t-\tau)_{ii} & \boldsymbol{h}(t-\tau)_{ij}\\ \boldsymbol{h}(t-\tau)_{ji} & \boldsymbol{h}(t-\tau)_{jj}\end{bmatrix}\begin{Bmatrix}\dot{\xi}_i\\ \dot{\xi}_j\end{Bmatrix}d\tau \tag{21}$$

The coupled time-domain analysis was performed with an in-house code using FORTRAN to predict the motions of side-by-side vessels under different wave directions. The fourth-order Runge-Kutta method is used to solve the partial differential equation. Because it is different from single-body calculation, multibody time-domain simulation faces a great challenge of convergence aroused by gap water resonance. The accurate calculation of retardation function is vital to the convergence of the time-domain solution and will be extensively explained in the following section.

Improvement of Retardation Function

In the time-domain analysis, retardation function influences the precedent fluid domain on the present ship motions. Normally, the Fourier cosine transformation, as the first expression in Eq. (19), is used to calculate the retardation function based on the frequency-domain potential damping for faster convergence. Hence, the quality of potential damping decides the outcome of retardation function. The potential damping of FLNG for both multibody (ε = 0/0.05) and single-body cases is illustrated in Fig. 2(a). The curves demonstrate the shape of delta function in the multibody case, with huge spikes at resonant frequencies induced by sloshing waves in the gap zone. Nevertheless, the introduction of nonzero ε reduces the peak value of spikes.

Following the ideal fluid assumption of Lewandowski (2008), the multibody potential damping can be represented in the form of the summation of single-body damping and delta function modification as

$$b(\omega) = b_1(\omega) + \sum_n C_n \omega_n \pi \delta(\omega - \omega_n) \tag{22}$$

where ω_n = critical frequencies $n = 0,1,2\ldots$; b_1 is the basic damping coefficient without resonance effect, which is qualitatively similar to the single-body potential damping; and C_n represents constants associated with the peak amplitudes. The Fourier cosine transformation of Eq. (22) can be written as follows:

$$h(t) = h_1(t) + 2\pi \sum_n C_n \omega_n \cos(\omega_n t) \tag{23}$$

This means that the retardation function (ideal fluid) can be treated as the sum of the sinusoid component at each critical frequency superimposed on a normal memory function h_1 (single-body case), as shown in Fig. 2(b), when $\varepsilon = 0$.

Fig. 2(b) shows that the retardation function in the single-body case fully decays within 20 s, whereas it takes much longer for the multibody case (over 150 s). This is due to the wave reflection within the gap region without viscidity. The long-lasting oscillatory sinusoid component of the retardation function in multibody cases (Fig. 2, $\varepsilon = 0$) is undesired in time-domain simulation because it causes the accumulation of motion energy and divergence of results. Improvement should be made in frequency-domain results to simulate the dissipation of energy. The higher the ε introduced in the frequency-domain to suppress the resonance peak is [Fig. 2(a)], the faster the retardation function [Fig. 2(b), $\varepsilon = 0.05$] will decay, making it easier for time-domain simulation to converge in avoidance of unrealistic energy accumulation. In this study, a fine frequency interval of 0.005 rad/s and a high-frequency truncation up to 3 rad/s are used in the integral of retardation function. The retardation function with ε = 0.05 gets sufficiently damped; thus, it can be truncated at 300 s.

To help understand the calculation process, the flowchart of multibody frequency and time-domain simulation is made to clarify each step, as shown in Fig. 3.

Numerical and Experimental Models

Numerical Model

The frequency-domain model, incorporating the artificial damping method, of this side-by-side configuration was established to calculate the gap wave elevation RAOs, hydrodynamic coefficients, and motion responses of two vessels by using HydroStar. As we mainly focused on the hydrodynamic interactions under various wave headings, both vessels are floating freely in close proximity without mechanical coupling. The gap between the two bodies is set as 6 m constantly. The principal scantlings of the FLNG and LNGC are listed in Table 1. The wet-surface panel models of the side-by-side vessels are shown in Fig. 4; the number of elements for FLNG and LNGC are 2,808 and 1,916 after a check of the grid independence to ensure the convergence of solution.

Before the implementation of the artificial damping method, the right artificial damping coefficient ε and the size of the free-surface damping zone need to be determined. Nevertheless, a uniquely precise definition of the free surface in the gap zone is often not possible, particularly when the two geometries are dissimilar as in the present study. The selection of ε is also somewhat empirical and mainly determined through tuning with test results. The effectiveness of this method can be justified only if the tuned ε, after implementation of the artificial damping method, can suppress the drastic free-surface motions near resonant frequencies.

In this study, a fixed value of ε on the entire gap area following the method of Watai et al. (2015) was decided by tuning the wave elevations from numerical simulation with experimental data. The area of the free-surface grid in this study covers the gap region along the parallel midsection of LNGC in which 144 panels are generated, as seen in Fig. 4.

To take into account the viscous drag of the roll motion, the linear viscous damping coefficient of roll motion was added into the motion equation in both the frequency and time domain, respectively. The frequency-domain roll damping coefficient can be derived from the time series of decay tests in still water according to

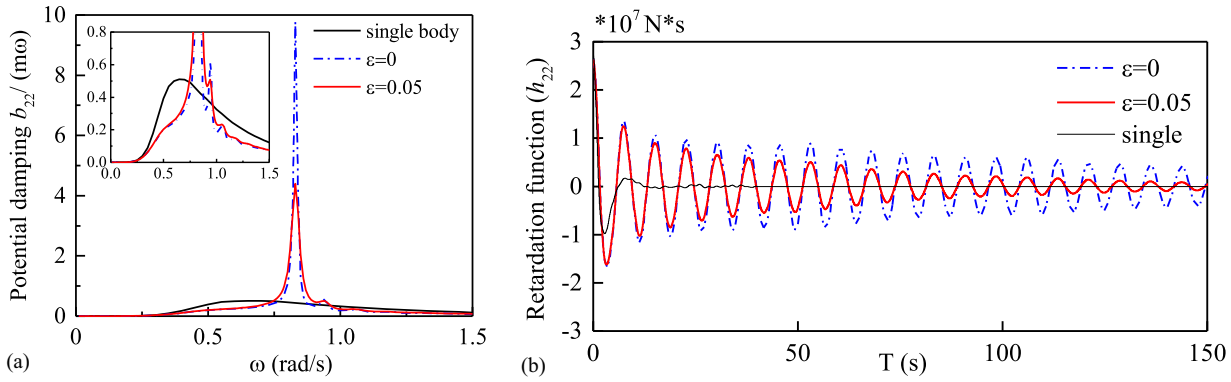

Fig. 2. (a) Damping coefficients and (b) retardation function for FLNG in the sway mode.

J. Waterway, Port, Coastal, Ocean Eng., 2018, 144(4): 04018007

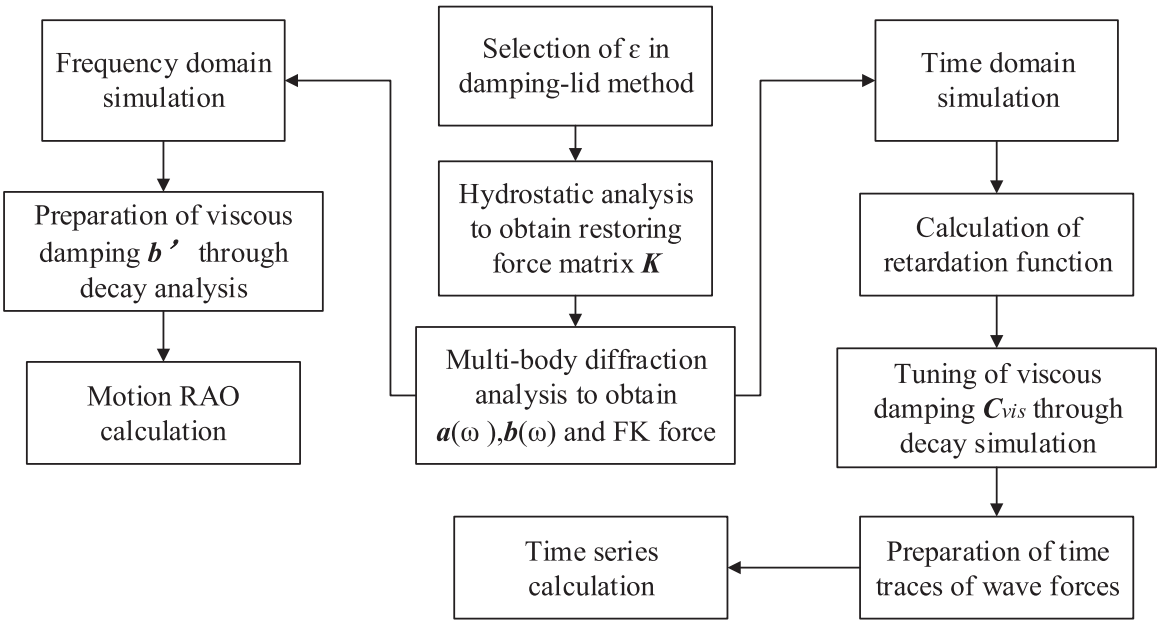

Fig. 3. Flowchart of multibody hydrodynamic calculation.

Table 1. Principal particulars of the FLNG and LNGC carrier

Designation	Unit	FLNG	LNGC
Length overall (Loa)	m	213.94	171.152
Breadth (B)	m	44.8	35.84
Depth (D)	m	25.5	20.4
Draft (T)	M	10.8	9
Displacement weight (Δ)	T	98,923.1	52,821.3
COG from keel (VCG)	m	13.8	12
Roll radius of gyration (Rxx)	m	16	10.2
Pitch radius of gyration (Ryy)	m	60	50
Heave natural frequency	rad/s	0.97	1.04
Roll natural frequency	rad/s	0.48	0.56
Pitch natural frequency	rad/s	0.60	0.66

Note: COG = center of gravity; VCG = vertical center of gravity.

Zhao et al. (2013). While in the time domain, the appropriate roll damping added into the time-domain motion equation can be achieved by tuning the calculated decay curves with the test results according to Xu et al. (2015).

Experimental Setups

To provide experimental validations and determine the important viscous damping terms that cannot be calculated, model tests of side-by-side FLNG and LNGC were performed in the deepwater offshore basin at Shanghai Jiao Tong University. The models were made at a scale of 1:60 according to Froude scaling principle.

Fig. 5 illustrates the layout of two parallel vessels at a distance of 6 m in full-scale. The midship sections of two vessels are both at the zero point on the *x*-axis of the global coordinate system (Fig. 4) so that the multibody system is longitudinally symmetric. Each floating body was horizontally moored with four soft springs, two at the bow with 45° and two at stern with 45°. The soft mooring system is used to prevent the second-order drift motions and fix their headings. The stiffness of each spring is small enough to keep the natural periods of vessels' horizontal motions far longer than wave periods.

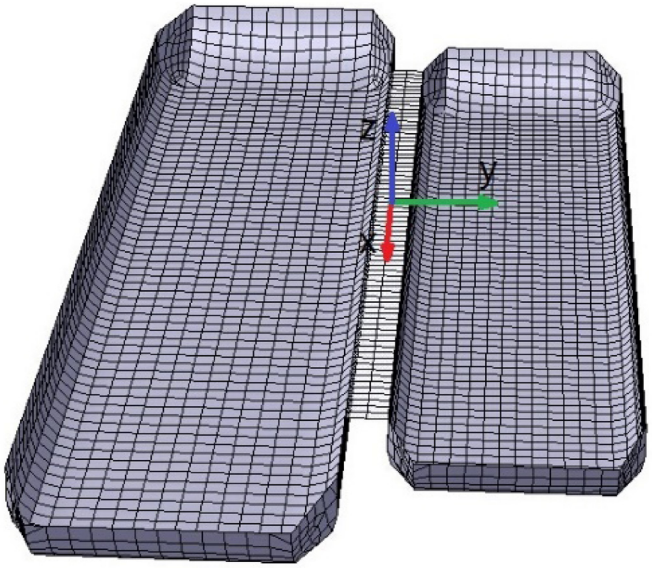

Fig. 4. Side-by-side arrangement of parallel bodies and mesh of gap surface.

As a result, no interference between wave frequency motions and low-frequency motions would be caused by mooring lines. To prevent collisions and protect the models in tests, two identical fenders (Fig. 5, black strips), without any hawser, were placed symmetrically about the midship on the interior water plane, whereas in the numerical simulation no mechanical coupling is taken into account. The longitudinal distance between the fender and midship is 46 m, and the linear stiffness is 885.6 KN/m. The fenders were attached to FLNG with no pretension and had little influence on the couplings between vessels because collisions, in fact, rarely occurred in the mild wave conditions.

For the environmental condition, only waves were included without wind or current. The tests were performed in a water

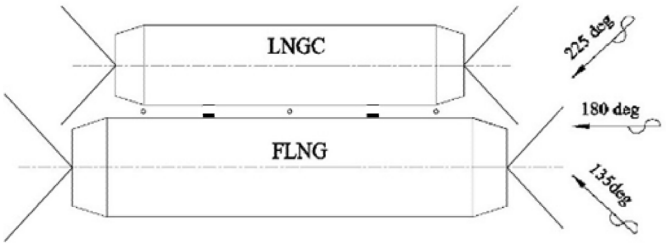

Fig. 5. Top view of the test setup and wave headings.

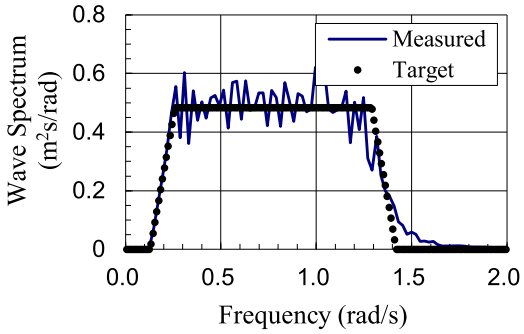

Fig. 6. Spectrum of white noise waves (full-scale).

depth of 5 m, corresponding to the water depth of 300 m in reality. The white noise waves, in full-scale, had a significant wave height of 3 m to meet the linear assumption and wave frequencies ranging from 0.25 to 1.25 rad/s to cover the main response frequencies of floaters. Each test was run for a duration of 3 h. The same white noise wave spectrum was adopted in model tests incoming from three different angles, 135, 180, and 225°, as illustrated in Fig. 5. Calibration of white noise wave spectrum is shown in Fig. 6.

The tests included decay tests and white noise wave tests. In white noise wave tests, resistance-type wave probes were used to measure wave elevations in the gap. They were set longitudinally at the beginning, end, and middle of the parallel midsection of LNGC along the gap central line, as illustrated with the tiny circles in Fig. 5. Motions of each vessel were measured by the noncontacting laser pointer finder. The RAOs of wave elevations and motions of 6 DOF can be obtained through spectral analysis of measured time series. The wave elevation RAOs can be used to tune the artificial damping ε to suppress unrealistic wave elevations in simulation, whereas the motion RAOs of both vessels can be used to validate the numerical model.

Results and Discussions

Calibration of Numerical Model

For better accuracies, the numerical model was calibrated by test results to determine the artificial damping ε and viscous damping in certain modes. First, the artificial damping ε should be tuned through gap wave elevations, and the frequency-domain viscous damping can be obtained from decay analysis (Table 2). Based on the frequency-domain hydrodynamic coefficients under proper ε, the time-domain viscous damping could then be selected with the measured decay curves.

Table 2. Results of roll decay tests

Designation	Natural period (s)	Nondimensional damping coefficient
FLNG	13.08	0.0114
LNGC	11.22	0.0122

Artificial Damping Method Application

The selection of damping coefficient ε in Eq. (13) is vital to suppress the resonant amplitude of gap waves to the realistic value. A great deal of work has been done to study the determination of ε. Watai et al. (2015) found that the ε fitting the test results best tends to be larger if a narrower gap width existed. Lu et al. (2010) observed that the artificial damping method generates results in reasonably good correlation with the test results for a fairly wide range of damping coefficient values, suggesting that reasonable numerical results could be obtained even if the damping coefficient was not precisely tuned.

In most studies for a given gap width, a constant artificial damping ε can be used to match the test results in heading waves. Nevertheless, it is unknown whether the value of ε is susceptible to the change of wave directions, which remains to be validated in the present study.

Following the ε-selecting scheme presented in Chen (2011), wave elevations measured at the center of the gap can be used to tune the numerical model. Wave elevations calculated based on four values of parameter ε (0,0.02,0.04,0.05) for each wave heading have been compared with test results at the gap center in the present study. Fig. 7 shows that although under different wave directions (135,180,225°), ε between 0.04 and 0.05 can give the numerical result that fits the experimental data best. For the convenience of further study, $\varepsilon = 0.05$ is selected to implement calculations despite various wave headings.

From Fig. 7, one observes that the increase of ε indeed suppresses the amplitude of wave elevations in certain frequencies at a constant interval and causes less effect over the rest frequencies. Extensive works on the resonant phenomenon of gap water have been performed by Lewandowski (2008) and Sun et al. (2015). These critical frequencies, following the definition by Lewandowski (2008), correspond to the natural modes of free-surface elevation in the gap zone. The amplification and cancellation are attributed to the superposition of incoming waves, diffraction waves, radiation waves of ship motions, and most importantly, resonant waves between gap exits dividing the open water and gap region.

In addition to a brief analysis of gap water resonance, some interesting phenomena are also observed in Fig. 7. First, wave elevations under oblique seas [Figs. 7(a and c)] show small fluctuations at frequencies of 0.48 and 0.56 rad/s, which correspond to the roll natural frequencies of FLNG and LNGC, respectively. This reveals a weak coupling effect, which is even negligible in engineering, between wave elevations and roll motions of two vessels under oblique waves. Second, the amplitude of wave resonance under waves of 225° is much larger than that under waves of 135°. This possibly arises from the shielding effect of FLNG on the weather side under 135° waves, which reflects most incoming waves to keep the gap region less disturbed. Third, the frequency shift between the numerical and test results at resonant frequencies is observable but only with a small discrepancy (about 0.02 rad/s), which also justifies the accuracy of the grid density according to Bunnik et al. (2009).

Decay Tests

In decay tests of roll and pitch mode, moments of inertia of models have been validated through the measurement of natural frequencies.

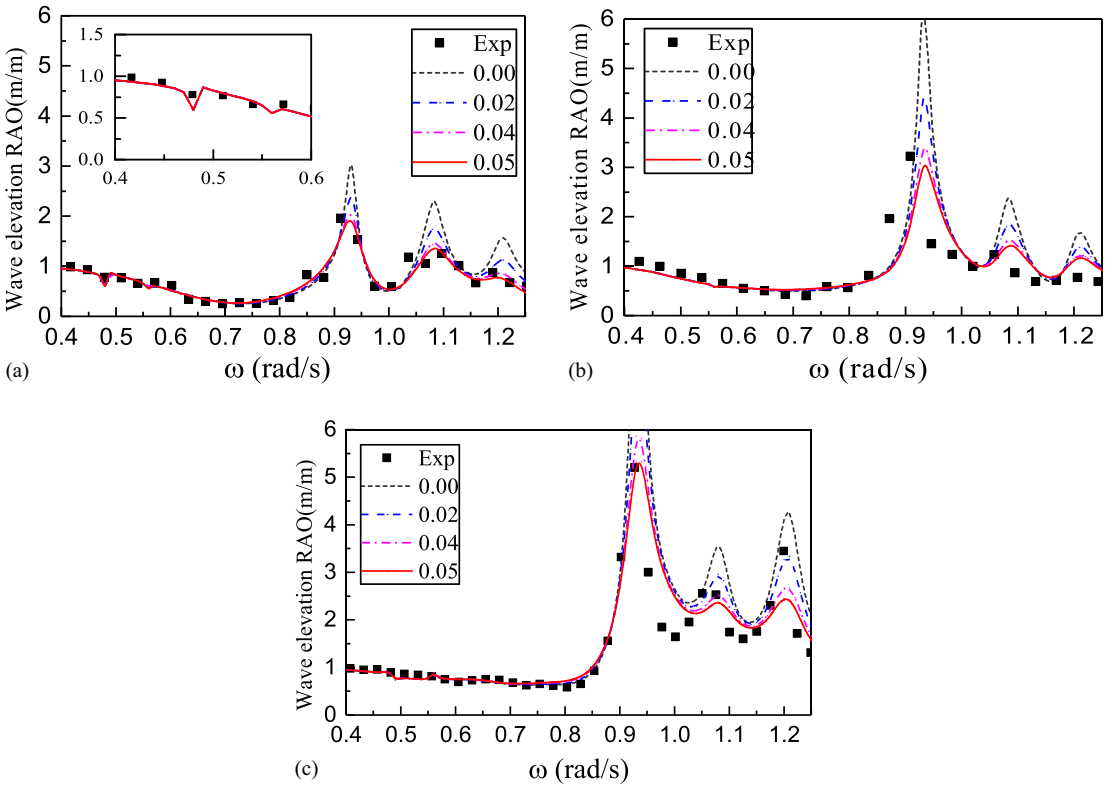

Fig. 7. Comparison of wave elevation at the gap center between numerical and test results: (a) 135°; (b) 180°; (c) 225°.

Among all modes, the roll viscous damping is the most important because its value is comparable with the radiation damping and must be considered in numerical simulation. Results of roll decay analysis are shown in Table 2, in which the damping coefficient refers to the linearized damping ratio with respect to the critical damping.

Based on the in-house time-domain code, an appropriate roll viscous damping [C_{vis} in Eq. (18)] could be determined by simulating the decay of either vessel while the other one is fixed. The accuracy of the code is also validated through the comparison between numerical and test decay results.

The decay results of model tests and numerical simulation are compared for both FLNG and LNGC in roll and pitch modes, as shown in Fig. 8. Through sharing the same periods, the calculated roll decay curves [Figs. 8(a and b)] without viscous damping decay slower than the test results. The application of appropriate roll viscous damping makes two vessels decay faster to match the test results precisely. The roll viscous damping coefficients are tuned by matching the calculated decay curves with the test results, which are 2.9×10^8 Ns/m for FLNG and 1.2×10^8 Ns/m for LNGC in the time-domain simulation. For the pitch decay curves, a fairly good agreement can be directly achieved between numerical and test results in Figs. 8(c and d). Hence, no extra viscous damping is needed in the pitch mode because the radiation damping generated by pitch motion is far more important than the viscous damping, as opposed to the roll mode in which the viscous damping is equally important. The natural pitch period is 10.5 s for FLNG and 8.8 s for LNGC.

Hydrodynamic Performances under Oblique Waves

Frequency-domain analysis is used to investigate the side-by-side system's motion responses of all DOF. To develop a qualitative understanding of hydrodynamic interactions under oblique waves, motion responses under oblique waves are studied first through a comparison between numerical and test results.

A typical oblique wave direction of 135° is selected to reveal the features of motion under oblique waves, and the results are illustrated in the Figs. 9 and 10. Fig. 9 shows the surge, heave, and pitch results of FLNG (on the right side) and LNGC (on the left side), respectively, and Fig. 10 shows the roll, pitch, and yaw results. All motion responses are normalized by incidental wave amplitude and plotted against frequency (rad per second). Numerical results of different values of ε are presented for the comparison with experimental results (black dots).

Fig. 9 shows that motion responses show similar trends for both ships, with a lower amplitude for FLNG because of its large inertia. Gap water resonance imposes little influence on the motion responses of the three modes at frequencies from 0.9 to 1.1 rad/s, with only small variations for LNGC in heave and pitch modes around 1 rad/s. For the heave motion of FLNG, it is noticeable that a slump of the curve occurs at the roll natural frequency of LNGC and vice versa. This indicates that weak hydrodynamic couplings exist between the heave motion and other floater's roll motion, which is a main difference from the motion responses in head seas. Nevertheless, an overall agreement of numerical and experimental results can be achieved despite the change of ε.

In Fig. 10 it is indicated that the effect of gap water resonance on motion responses of sway and yaw is quite obvious at high frequencies. The application of $\varepsilon = 0.05$ successfully suppresses the impulsive motion responses at gap resonance frequencies, as shown in the subplots of sway and yaw motion, which justifies the effectiveness of the artificial damping method in the prediction of motion responses. The numerical model tends to slightly overestimate the peak value of roll resonance despite adding linearized viscous

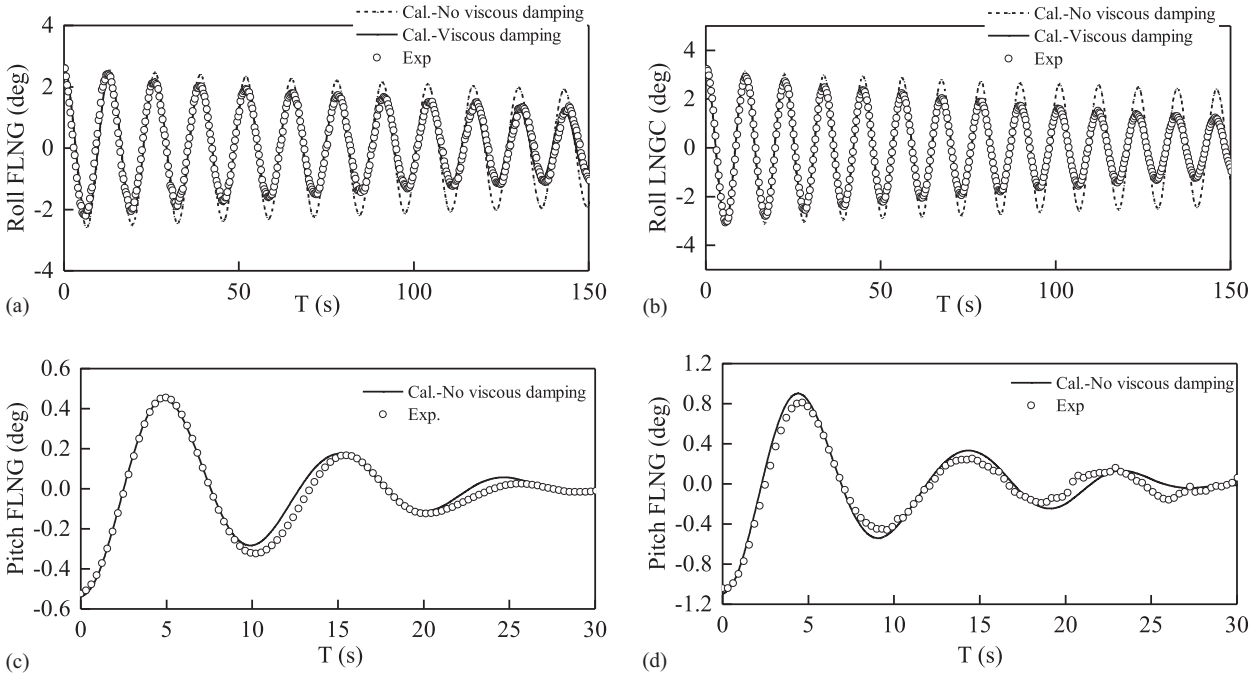

Fig. 8. Comparison of decay test results for FLNG and LNGC: (a) roll-free decay of FLNG; (b) roll-free decay of LNGC; (c) pitch-free decay of FLNG; (d) pitch-free decay of LNGC.

damping. This is induced by the nonlinearity of roll viscous damping at the natural frequency (Jung et al. 2006). Couplings between roll resonance and sway motion recur for both vessels so that a fluctuation of the sway RAO is observable at two roll natural frequencies.

Therefore, it is concluded that two features are obvious for multibody motion responses under oblique waves: (1) the coupling effects between roll motion and other modes and (2) the strong resonant motions at high frequencies induced by gap wave sloshing. Even though the coupling effects from roll resonance might be weak, they would induce unfavorable resonances of relative sway and heave motions between two hulls, as shown in discussions of relative motions.

Because of the different displacements of the two vessels, hydrodynamic performances under symmetrical oblique waves are not identical. To illustrate the influence of wave directions, motion responses under symmetric wave directions (135°/225°) are further calculated based on the constant value $\varepsilon = 0.05$. Comparisons of motion responses under different wave directions are plotted in Figs. 11 and 12, in which the single-body case refers to the condition of only FLNG or LNGC in quartering seas without multibody interaction.

It is first observed that the amplitudes of the transversal motions of sway, roll, and yaw (Fig. 12) under head seas are much smaller for both vessels. Thus, the head sea is the most ideal wave condition for side-by-side configuration.

For the oblique wave conditions (135°/225°), Figs. 11 and 12 show that motion responses of FLNG are insusceptible to the change of wave directions due to its large inertia. The low frequency responses ($\omega < 0.45$ rad/s) of LNGC are similar to a single body under either 135° or 225° waves, showing no hydrodynamic disturbance. This is because low-frequency waves have a strong transmission effect and cause weak hydrodynamic interactions between hulls. With the increase of incoming wave frequency, LNGC bears smaller motions at the lee side (135°), especially for heave, pitch, and yaw motion. This can be explained by the shielding effect of FLNG because once FLNG is at the weather side (135°), the reflection effect dominates at high wave frequencies so that less wave energy is absorbed by the lee side LNGC. The same phenomenon was also observed by Kim et al. (2008).

A spatial phenomenon associated with sway and yaw motions (Fig. 12) shows that regardless of wave directions, LNGC at either the lee side or weather side generates smaller motion amplitude than that in the single-body case. A huge FLNG can act as a shielding obstacle at the weather side or a quay at the lee side, both of which serve to stifle the motion responses of LNGC. This is a favorable behavior because LNGC in the side-by-side configuration has smaller transversal motion responses.

At resonance frequencies featured by sloshing waves in the gap, greater motion responses of FLNG and LNGC can be found under 225° wave direction in sway and yaw modes (Fig. 12). This behavior concurs with the trend of gap wave elevations under various wave directions. Being exposed to the 225° waves, the motion of the weather-side LNGC is significantly amplified by the drastic resonant waves at frequencies between 0.9 and 1.2 rad/s.

Relative Motions under Different Wave Directions

Relative motion between two hulls is an important issue in side-by-side configuration because offloading arms are sensitive to the relative motions between two vessels. Time-domain calculation is implemented to study the relative motions between two vessels under oblique waves, which is defined in Eq. (24) as the motion of body i with respect to body j in 6 DOF

$$\xi_{R_{ij}}(t) = \left[\xi_i(t) - \xi_j(t)\right], \xi(t) = \begin{Bmatrix} \xi_i(t) \\ \xi_j(t) \end{Bmatrix} \tag{24}$$

The RAOs of relative motions in all modes are calculated at each frequency with the in-house code and compared with experimental results under two typical wave directions, as shown in Fig. 13. The test results of the 135° oblique wave and head wave are presented

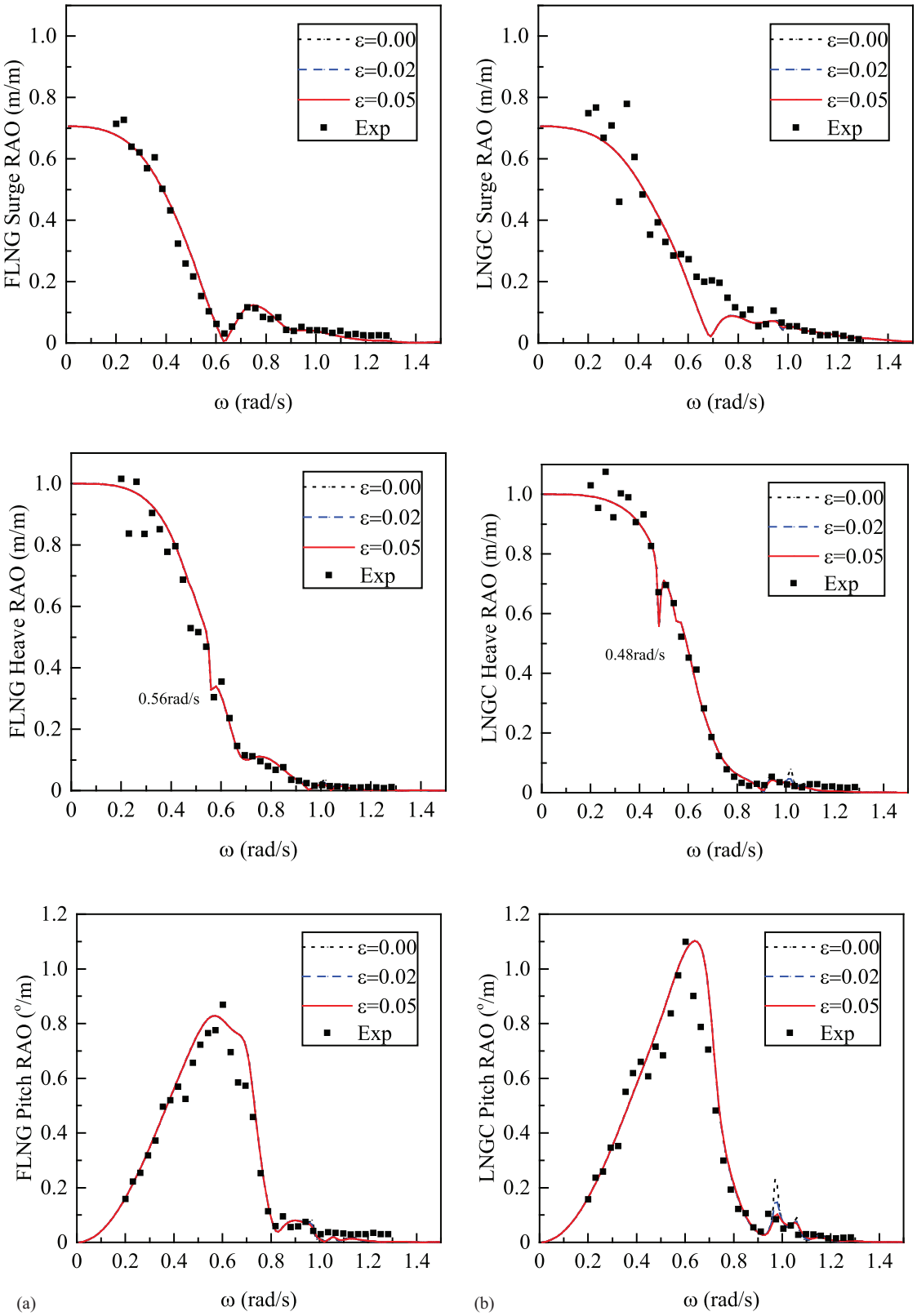

Fig. 9. Surge, heave, and pitch motion RAOs for (a) FLNG and (b) LNGC under the oblique wave of 135°.

for validation. Large discrepancies between the 180° experimental and numerical results of sway and yaw motion are observed at low frequencies. This could be explained by the nonexact head waves in model tests, as opposed to the numerical simulation. Although held at the correct heading, two vessels are inevitably rotated by the small yaw motions in model tests to increase the transversal wave loads on hulls, as well as the consequent sway and yaw motions.

Nevertheless, Fig. 13 demonstrates an overall agreement between numerical and experimental results in terms of the trend and magnitude for most modes, except for relative surge motion, in

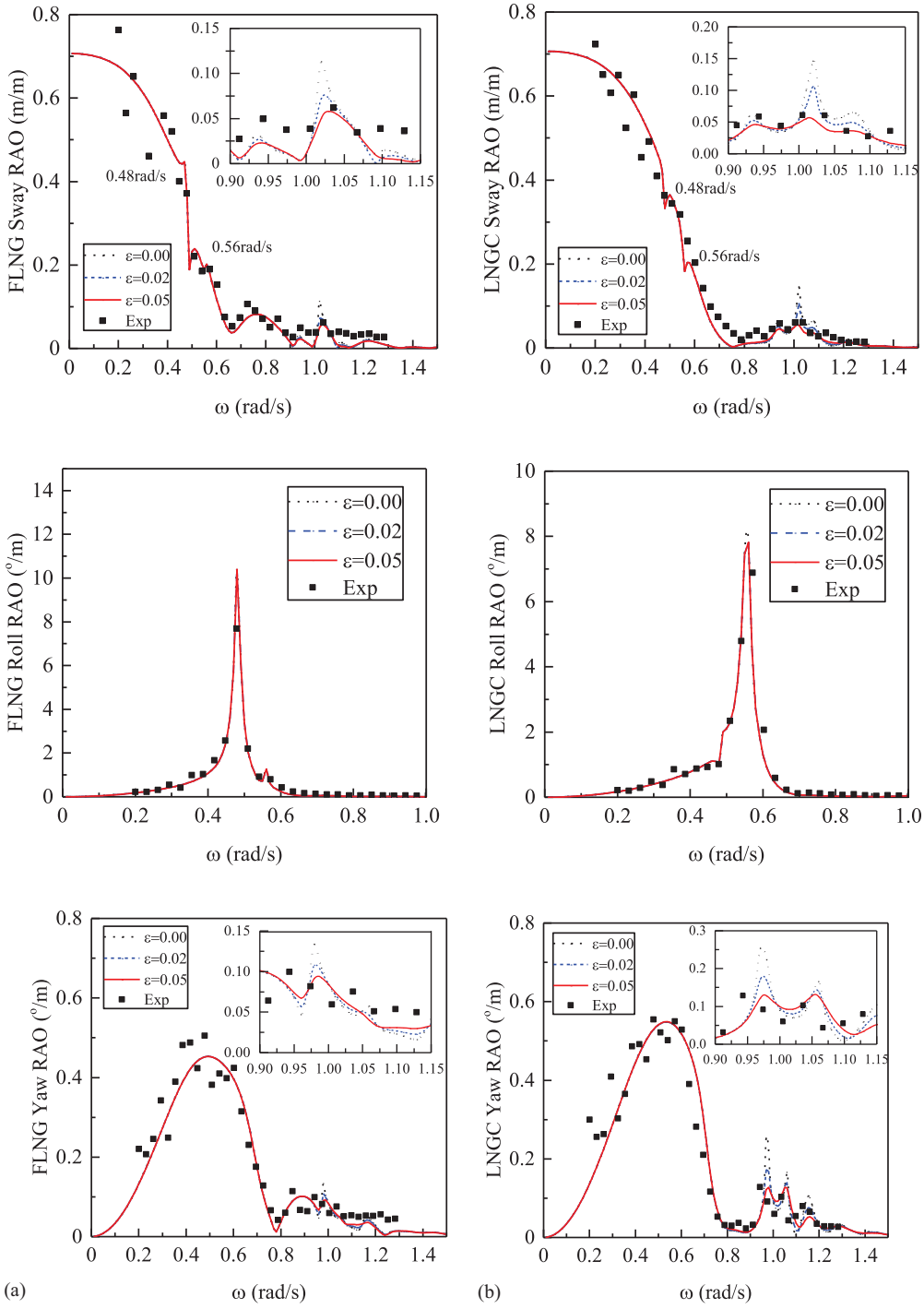

Fig. 10. Sway, roll, and yaw motion RAOs for (a) FLNG and (b) LNGC under the oblique wave of 135°.

which a large discrepancy also occurs at low frequencies. The reason for this discrepancy is unclear. Because of the overall concurrence of the absolute surge amplitude (Fig. 9), it is conjectured that the phase shift associated with surge damping might be responsible. In model tests the rotation of floaters due to yaw motions would change their original surge damping, causing variation of the motion phase angle subsequently. Hence, the measured relative surge motion obviously differs from the one calculated based on the linear assumption that neglects the rotation of bodies. This explanation also can be supported by the phenomenon that, with the decrease of yaw motions at high frequencies (>0.8 rad/s), the calculated relative surge motion matches well with the test results.

Relative motions under head sea conditions are much smaller compared with those under oblique waves (Fig. 13), justifying the favorable wave direction among all. For example, the relative roll resonance reaches its maximum of 6.74° under the 135° oblique wave, whereas it reaches only 1.75° under the head sea. For the oblique waves, the relative motion responses of surge, heave, and pitch motion demonstrate a highly damped mode. Under the wave direction of 135°, relative pitch is smaller than that under a 225° wave due to the shielding effect of FLNG on LNGC. Spikes in relative heave and sway motion are aroused from strong couplings with roll resonance. Peaks of the relative roll motion are associated with roll resonance of both ships, and

J. Waterway, Port, Coastal, Ocean Eng., 2018, 144(4): 04018007

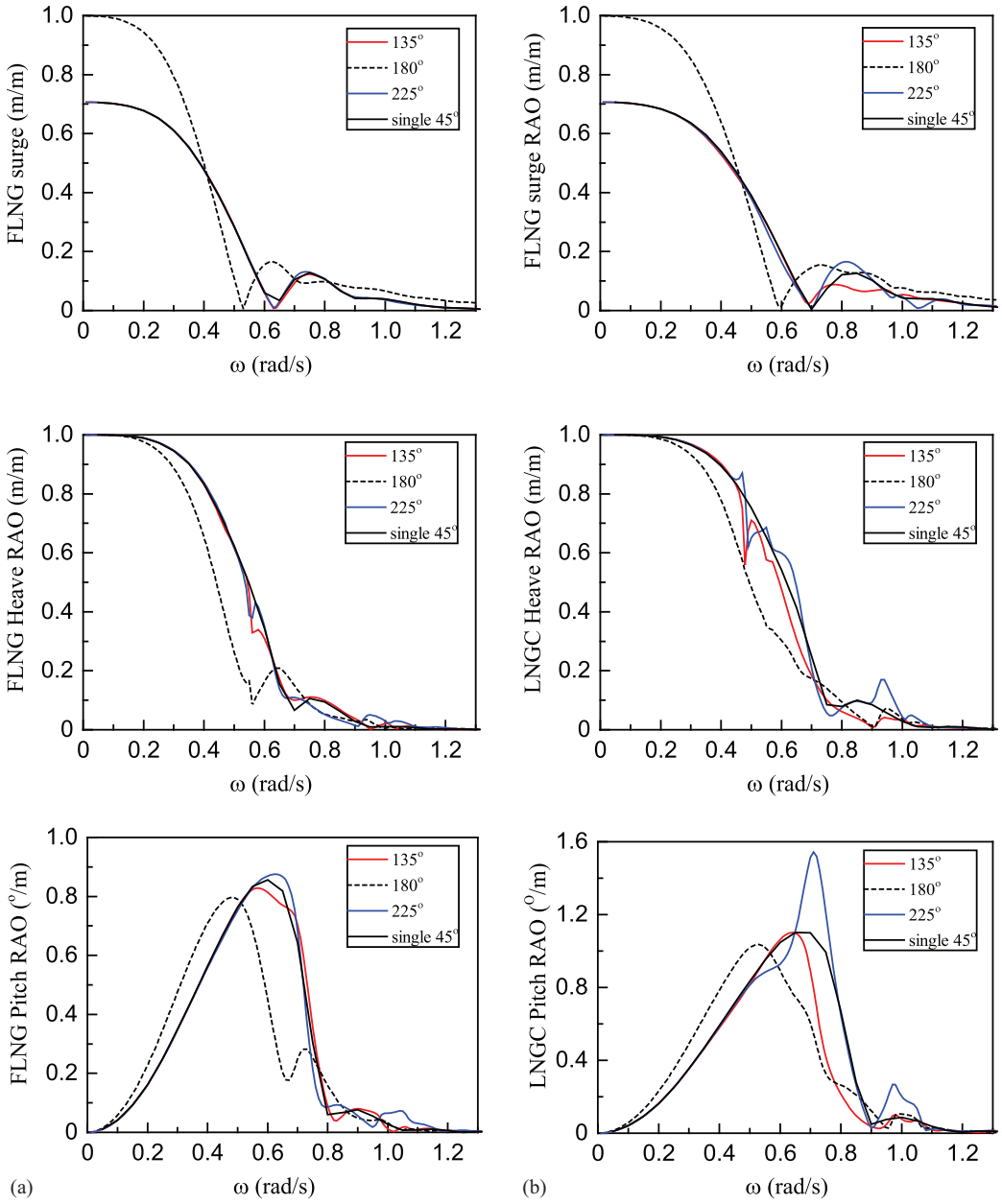

Fig. 11. Surge, heave, and pitch motion RAOs for (a) FLNG and (b) LNGC under different wave directions.

the amplitudes are bigger when LNGC is on the weather-side (225° wave).

At high frequencies, the influence of gap water resonance on relative motion is obvious for sway and yaw motions, especially when LNGC is at the weather-side (225° wave). Fig. 14 shows the time series of relative sway and yaw motion for the regular wave parameter $\omega = 1.05$ rad/s (resonance frequency) and $\xi_a = 1$ m. It brings greater risks of collision when two vessels oscillate in opposed directions, which results in more intensive relative motions.

To further analyze the resonant peaks of relative motion, a phase shift analysis based on numerical results is implemented hereafter. The absolute phase shifts of relative motions, together with relative motion RAOs, are presented in Figs. 15 and 16. The out-of-phase and in-phase relative motions, following the definition by Voogt and Brugts (2010), account for the natural modes of relative motions. The in-phase mode means both bodies moving together when the phase shift approaches zero, whereas the out-of-phase mode means they move in opposed directions when the phase shift approaches 180°.

In Fig. 15, relative heave motions of both oblique waves show no sharp resonant peak, although the coupling effect of roll resonance is noticeable. For the relative roll motion, it is observed that the in-phase and out-of-phase resonant modes can, respectively, explain the peaks at frequencies 0.48 and 0.56 rad/s for two different oblique waves. Therefore, the roll resonance of FLNG, whose natural roll frequency is 0.48 rad/s, is quite dangerous and may give rise to a lateral collision, especially under a 225° wave direction.

For the relative sway and yaw motions in Fig. 16, the resonant peaks at high frequencies induced by gap water sloshing demonstrate a dangerous out-of-phase behavior. This could be explained because the amplified free-surface elevation between two hulls tends to dispel and draw back the two vessels in opposed directions periodically. As a result, it is safer to subject the FLNG against the incoming oblique wave at the weather side when the resonant free-

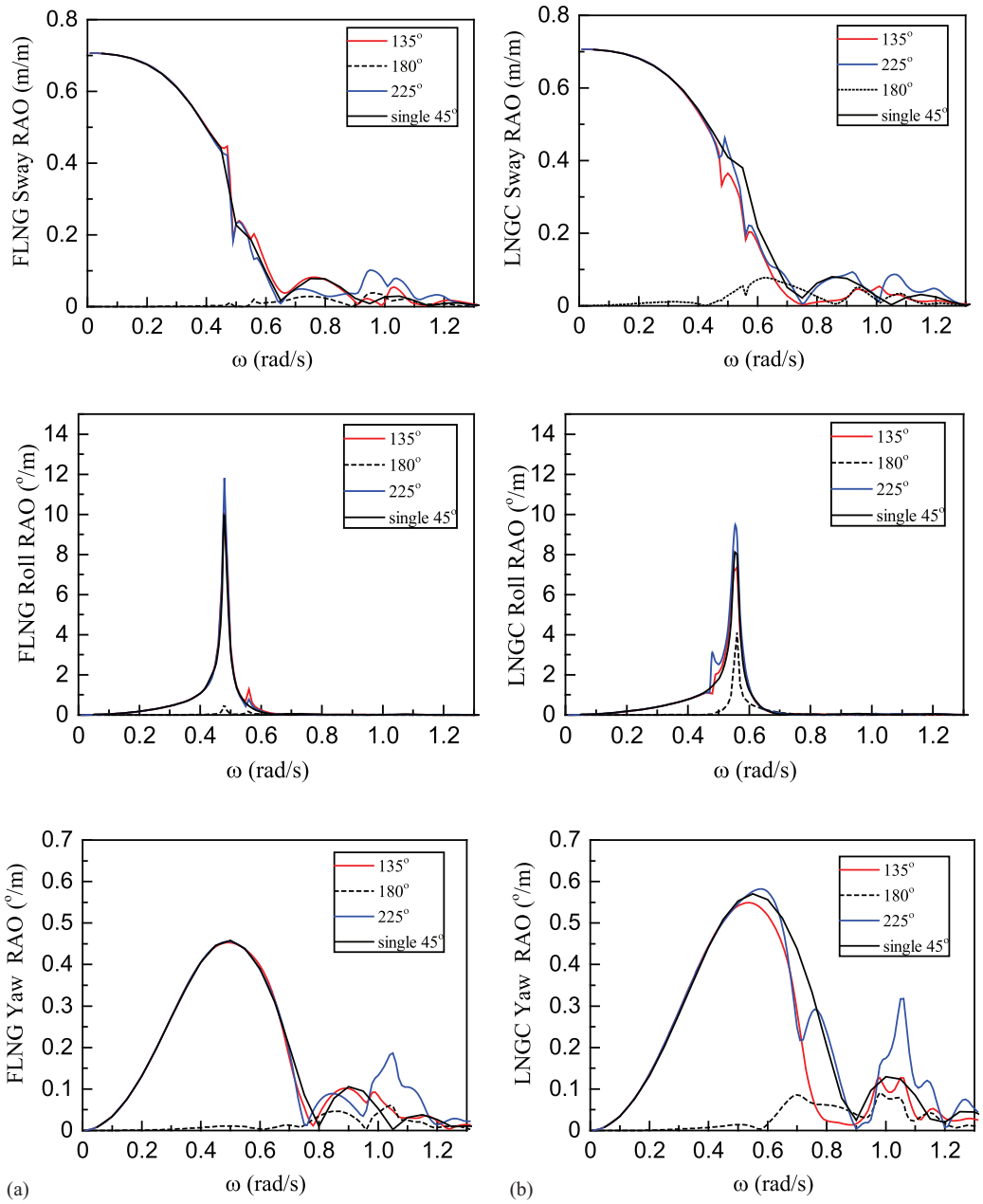

Fig. 12. Sway, roll, and yaw motion RAOs for (a) FLNG and (b) LNGC under different wave directions.

surface elevations are effectively suppressed, as well as the transversal relative motions of sway and yaw.

For the sharp peak of relative sway motion aroused from couplings with FLNG roll resonance, the phase shifts dependent on different wave directions decide the relative motion predominantly. Note that the out-of-phase mode happens under the 225° wave direction and the in-phase mode happens under the 135° wave direction. This indicates that drastic relative sway motion will be caused when oblique waves come from the side of LNGC (225°) with considerable energy around the FLNG's roll resonance frequency.

The previously mentioned resonance frequencies of relative motions are categorized and listed in Table 3. The numbers in bold represent the roll resonance of FLNG (0.48 rad/s) or LNGC (0.56 rad/s), whereas the rest are associated with gap water resonance. The out-of-mode relative motions are always triggered by gap water resonance under any wave direction, whereas the mode of relative motion induced by roll resonance varies with different wave directions and resonance frequencies.

Conclusions

A numerical model of side-by-side FLNG and LNGC is established and calibrated with model tests. The artificial damping method is used to suppress drastic gap wave resonance and modify the hydrodynamic coefficients. Hydrodynamic performances under various wave directions are predicted and analyzed. Based on these performances, the following conclusions can be obtained.

For the artificial damping method used in this investigation, a constant value of ε is applicable for different oblique wave directions from 135 to 225°. The amplitude of gap waves are found smaller under the 135° wave because of the shielding effect of FLNG.

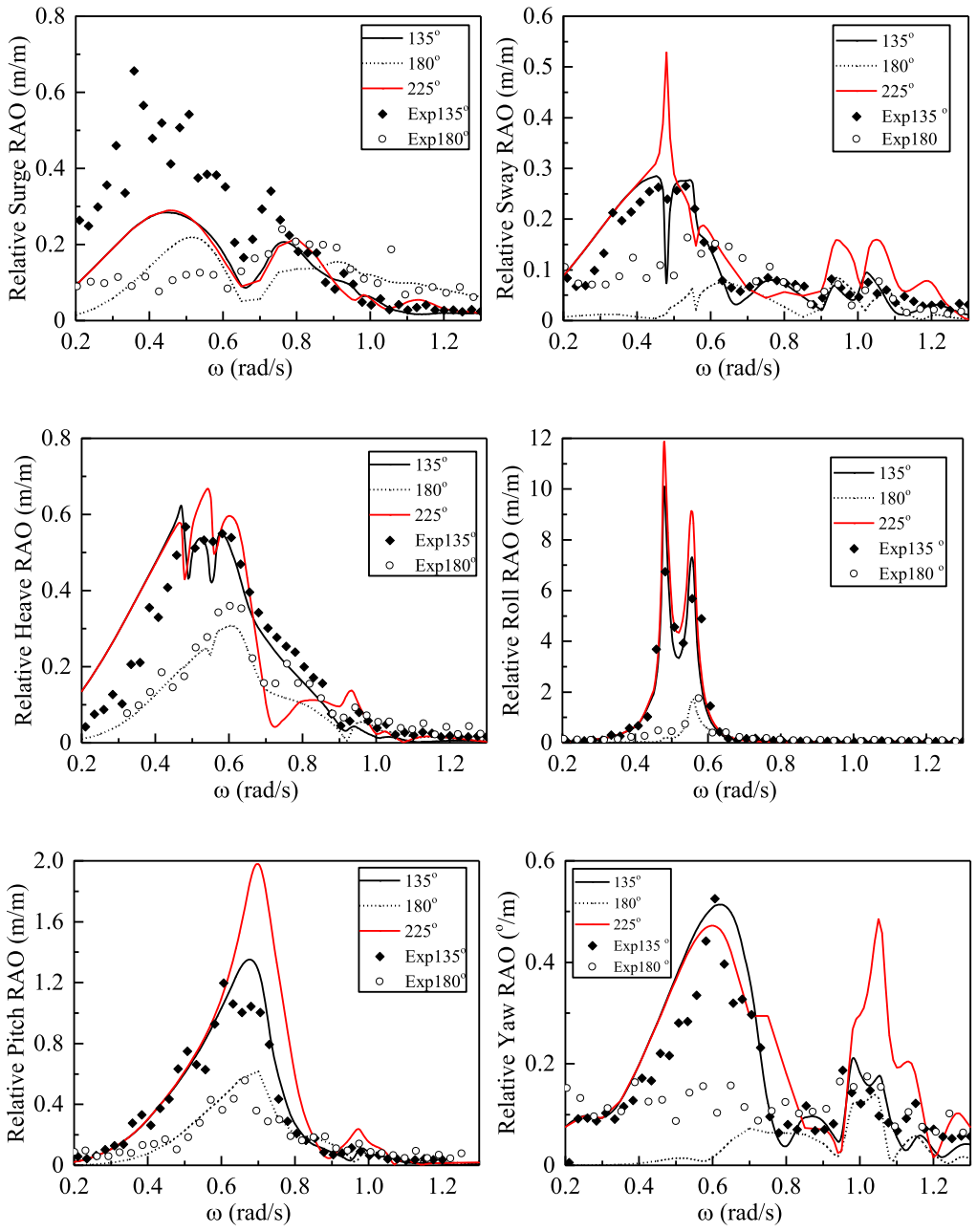

Fig. 13. Relative motion RAOs under different wave directions.

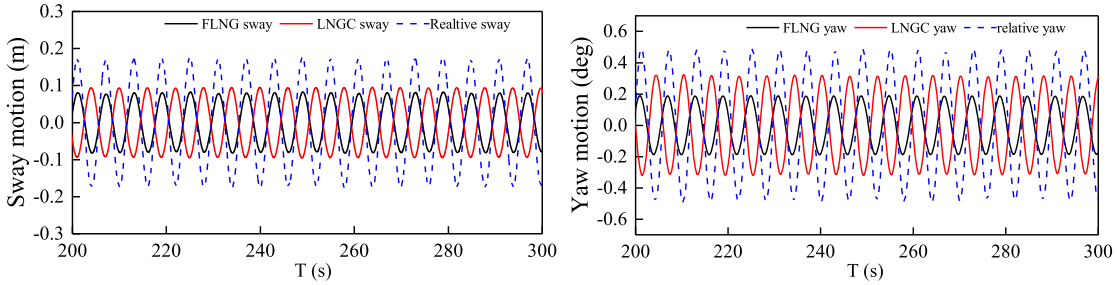

Fig. 14. Relative sway and yaw motion under the 225° regular wave ($\omega = 1.05$ rad/s, $\xi_a = 1$ m).

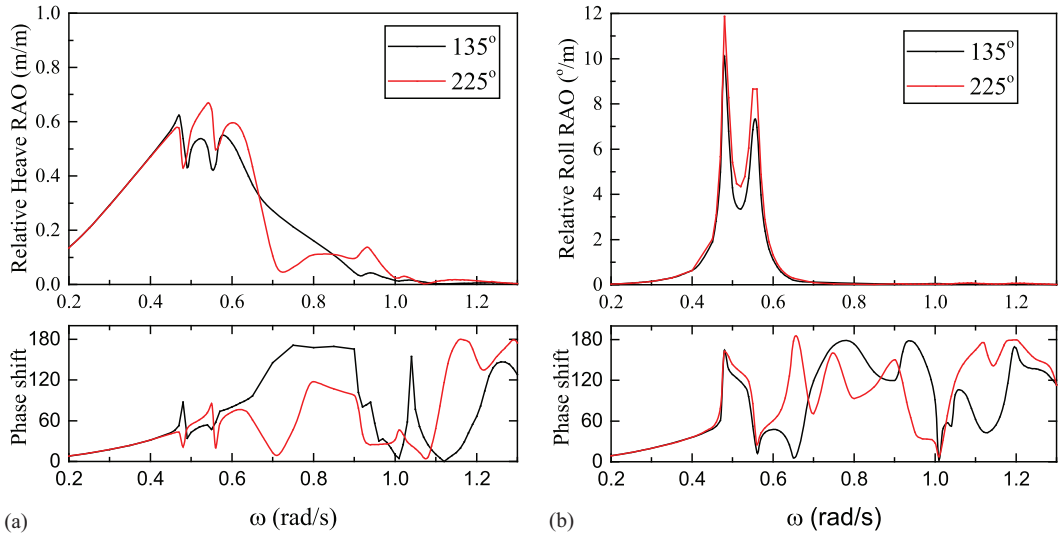

Fig. 15. Phase shift of relative (a) heave and (b) roll motion under oblique waves.

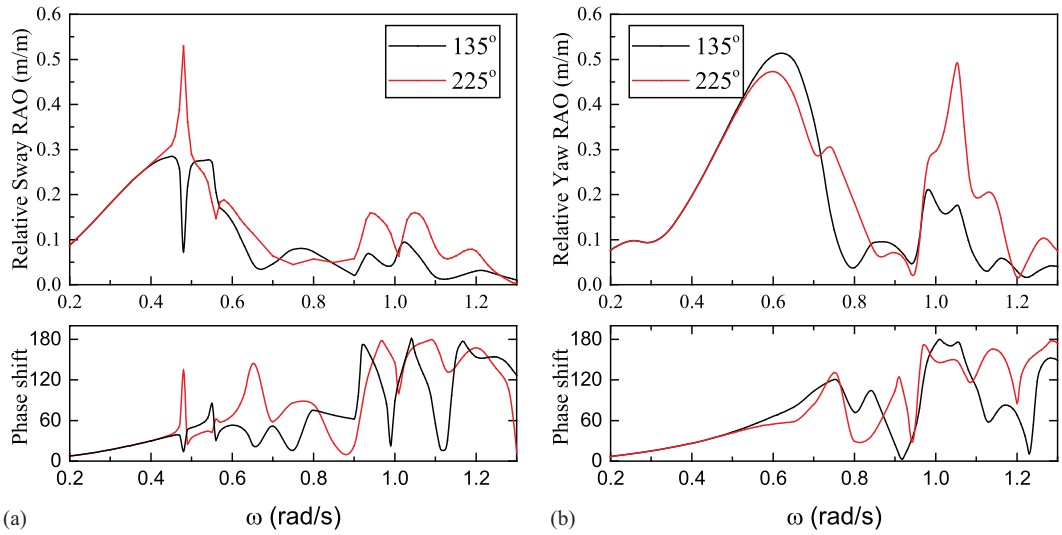

Fig. 16. Phase shift of relative (a) sway and (b) yaw motion under oblique waves.

Table 3. Relative motion resonance frequencies (rad per second)

	135°		225°	
Motion mode	In-phase	Out-of-phase	In-phase	Out-of-phase
Relative roll	**0.56**	**0.48**	**0.56**	**0.48**
Relative sway	**0.48**	0.93, 1.02	—	**0.48**, 0.95, 1.05
Relative yaw	—	0.97, 1.05	—	1.05

Note: The numbers in bold represent the roll resonance of FLNG (0.48 rad/s) or LNGC (0.56 rad/s).

With the finely tuned ε, the numerical model is able to predict the motion responses of two vessels under oblique waves, showing good agreement with model tests. Two spatial phenomena present the multibody hydrodynamics under oblique waves: (1) the couplings between roll motion and other modes and (2) strong resonant motions at high frequencies induced by gap wave sloshing.

Comparisons of motion responses under different wave directions show that motion responses of FLNG are insusceptible to the change of wave directions because of its large inertia, whereas motion responses of LNGC at the lee side (135°) are stifled due to the shielding effect of FLNG. Interestingly, LNGC at either the lee side or weather side has a smaller amplitude of sway or yaw motion than that in the single-body case because of the suppression effect of the FLNG aside.

Relative motions of all modes under different wave directions have been calculated and analyzed, showing good agreement with test results. Side-by-side vessels experience larger relative motions under oblique waves, particularly when LNGC is at the weather side. For the relative motion resonance, gap water resonance always enhances the relative motions with the out-of-phase mode, whereas the mode induced by roll resonance depends on wave directions and resonance frequencies.

To reveal the oblique wave effect on the FLNG system in a side-by-side an offloading operation, this study focuses on the hydrodynamics of the FLNG system due to variation of wave directions. Further research will incorporate the inner tank sloshing effect and the mechanical couplings to study the integrated hydrodynamic responses of the system under oblique waves.

Acknowledgments

This work was financially supported by the China National Scientific and Technology Major Project (2016ZX05028–002-004). This source of support is gratefully acknowledged by authors.

References

Buchner, B., A. Van Dijk, and J. De Wilde. 2001. "Numerical multiple-body simulations of side-by-side mooring to an FPSO." In Vol. 1 of *Proc., 11th Int. Offshore and Polar Engineering Conf.*, 343–353. Cupertino, CA: International Society of Offshore and Polar Engineering.

Bunnik, T., W. Pauw, and A. Voogt. 2009. "Hydrodynamic analysis for side-by-side offloading." In Vol. 3 of *Proc., 19th Int. Offshore and Polar Engineering Conf., Osaka, Japan*, 648–653. Cupertino, CA: International Society of Offshore and Polar Engineering.

Chen, X. 2005. "Hydrodynamic analysis for offshore LNG terminals." In *Proc., 2nd Int. Workshop on Applied Offshore Hydrodynamics*, Rio de Janeiro, Brazil.

Chen, X. 2011. "Offshore hydrodynamics and applications." *IES J. Part A* 4 (3): 124–142. https://doi.org/10.1080/19373260.2011.595903.

Choi, Y. R., and S. Y. Hong. 2002. "An analysis of hydrodynamic interaction of floating multi-body using higher-order boundary element method." In *Proc., 12th Int. Offshore and Polar Engineering Conf.*, Cupertino, CA: International Society of Offshore and Polar Engineering.

Cummins, W. E. 1962. *The impulse response function and ship motions*. Tech. Rep. Washington, DC: David Taylor Model Basin.

Fang, M., and G. Chen. 2001. "The relative motion and wave elevation between two floating structures in waves." In *Proc., 11th Int. Offshore and Polar Engineering Conf.*, 361–368. Cupertino, CA: International Society of Offshore and Polar Engineering.

Fournier, J. R., M. Naciri, and X.-B. Chen. 2006. "Hydrodynamics of two side-by-side vessels experiments and numerical simulations." In Vol. 1 of *Proc., 16th Int. Offshore and Polar Engineering Conf.*, 158–165. Cupertino, CA: International Society of Offshore and Polar Engineering.

Hong, S. Y., J. H. Kim, H. J. Kim, and Y. R. Choi. 2002. "Experimental study on behavior of tandem and side-by-side moored vessels." In *Proc., 12th Int. Offshore and Polar Engineering Conf.*, Cupertino, CA: International Society of Offshore and Polar Engineering.

Huijsmans, R., J. A. Pinkster, and J. J. De Wilde. 2001. "Diffraction and radiation of waves around side-by-side moored vessels." In *Proc., 11th Int. Offshore and Polar Engineering Conf.*, Cupertino, CA: International Society of Offshore and Polar Engineering.

Jung, K., K. Chang, and H. Jo. 2006. "Viscous effect on the roll motion of a rectangular structure." *J. Eng. Mech.* 132 (2): 190–200. https://doi.org/10.1061/(ASCE)0733-9399(2006)132:2(190).

Kim, K., Y. Kim, and M. Kim. 2008. "Time-domain analysis of motion responses of adjacent multiple floating bodies in waves." In *Proc., 18th Int. Offshore and Polar Engineering Conf.*, Cupertino, CA: International Society of Offshore and Polar Engineering.

Kodan, N. 1984. "The motions of adjacent floating structures in oblique waves." *J. Energy Resour. Technol.* 106 (2): 199–205. https://doi.org/10.1115/1.3231038.

Lewandowski, E. M. 2008. "Multi-vessel seakeeping computations with linear potential theory." *Ocean Eng.* 35 (11–12): 1121–1131. https://doi.org/10.1016/j.oceaneng.2008.04.011.

Lu, L., L. Cheng, B. Teng, and L. Sun. 2010. "Numerical simulation and comparison of potential flow and viscous fluid models in near trapping of narrow gaps." *J. Hydrodyn Ser. B* 22 (5): 120–125. https://doi.org/10.1016/S1001-6058(09)60180-3.

Molin, B. 2001. "On the piston and sloshing modes in moonpools." *J. Fluid Mech.* 430: 27–50. https://doi.org/10.1017/S0022112000002871.

Newman, J. N. 2004. "Progress in wave load computations on offshore structures." In *Proc, 23rd Int. Conf. Offshore Mechanics & Arctic Engineering*, New York: American Society of Mechanical Engineers.

Ohkusu, M. 1969. "On the heaving motion of two circular cylinders on the surface of a fluid." *Rep. Res. Inst. Appl. Mech.* 17 (58): 167–185.

Pauw, W. H., R. H. M. Huijsmans, and A. Voogt. 2007. "Advances in the hydrodynamics of side-by-side moored vessels." In *Proc., 26th Int. Conf. on Offshore Mechanics and Arctic Engineering*, 597–603. New York: American Society of Mechanical Engineers.

Pessoa, J., N. Fonseca, and C. Guedes Soares. 2015. "Numerical study of the coupled motion responses in waves of side-by-side LNG floating systems." *Appl. Ocean Res.* 51 (Jun): 350–366. https://doi.org/10.1016/j.apor.2015.01.012.

Shivaji, G. T., and D. Sen. 2016. "Direct time domain analysis of floating structures with linear and nonlinear mooring stiffness in a 3D numerical wave tank." *Appl. Ocean Res.* 51 (Jun): 153–170.

Sun, L., R. E. Taylor, and P. H. Taylor. 2015. "Wave driven free surface motion in the gap between a tanker and an FLNG barge." *Appl. Ocean Res.* 51 (Jun): 331–349. https://doi.org/10.1016/j.apor.2015.01.011.

Van der Valk, C. A., and A. Watson. 2005. "Mooring of LNG carriers to a weathervaning floater–side-by-side or stern-to-bow." In *Proc., Offshore Technology Conf.*, Offshore Technology Conference.

Van Oortmerssen, G. 1979. "Hydrodynamic interaction between two structures floating in waves." In *Proc., 2nd Int. Conf. on Behaviour of Offshore Structures (BOSS '79)*, London, 339–356.

Voogt, A. J., and H. Brugts. 2010. "SS: LPG & LNG offshore operations: Numerical simulations to optimize offshore offloading operations." In *Proc., Offshore Technology Conf.*, Offshore Technology Conference.

Watai, R. A., P. Dinoi, F. Ruggeri, A. Souto-Iglesias, and A. N. Simos. 2015. "Rankine time-domain method with application to side-by-side gap flow modeling." *Appl. Ocean Res.* 50 (Mar): 69–90. https://doi.org/10.1016/j.apor.2014.12.002.

Xu, X., X. Li, and J. Yang. 2016. "Hydrodynamic interactions of three barges in close proximity in a floatover installation." *China Ocean Eng.* 30 (3): 343–358. https://doi.org/10.1007/s13344-016-0023-9.

Xu, X., J. Yang, X. Li, and L. Xu. 2015. "Time-domain simulation for coupled motions of three barges moored side-by-side in floatover operation." *China Ocean Eng.* 29 (2): 155–168. https://doi.org/10.1007/s13344-015-0012-4.

Yeung, R. W., and R. K. M. Seah. 2007. "On Helmholtz and higher-order resonance of twin floating bodies." *J. Eng. Math.* 58 (1): 251–265. https://doi.org/10.1007/s10665-006-9109-3.

Zhao, W., J. Yang, Z. Hu, and L. Tao. 2014. "Prediction of hydrodynamic performance of an FLNG system in side-by-side offloading operation." *J. Fluids Struct.* 46 (Apr): 89–110. https://doi.org/10.1016/j.jfluidstructs.2013.11.021.

Zhao, W., J. Yang, Z. Hu, L. Xiao, and T. Peng. 2013. "Experimental and numerical investigation of the roll motion behavior of a floating liquefied natural gas system." *Sci. China Phys. Mech. Astron.* 56 (3): 629–644. https://doi.org/10.1007/s11433-012-4914-3.